AGU PUBLICATIONS

JGR

Journal of Geophysical Research: Oceans

RESEARCH ARTICLE

10.1002/2017JC012960

Key Points:
- A new regional NEMO model configuration of the North-Western European continental shelf at 1.8 km resolution is introduced
- This resolution allows the resolution of small-scale features such as internal tides, on the shelf and at the shelf break
- The spatial and temporal variability of the internal tides on the North-Western European continental shelf are investigated

Correspondence to:
J. Polton,
jelt@noc.ac.uk

Citation:
Guihou, K., Polton, J., Harle, J., Wakelin, S., O'Dea, E., & Holt, J. (2017). Kilometric scale modeling of the North West European Shelf Seas: Exploring the spatial and temporal variability of internal tides. *Journal of Geophysical Research: Oceans*, *123*, 688–707. https://doi.org/10.1002/2017JC012960

Received 3 APR 2017
Accepted 2 DEC 2017
Accepted article online 11 DEC 2017
Published online 30 JAN 2018

Kilometric Scale Modeling of the North West European Shelf Seas: Exploring the Spatial and Temporal Variability of Internal Tides

K. Guihou[1,2], J. Polton[1], J. Harle[1], S. Wakelin[1], E. O'Dea[3], and J. Holt[1]

[1]National Oceanography Centre, Liverpool, United Kingdom, [2]Servicio de Hidrografía Naval, Buenos Aires, Argentina, [3]Met Office, Exeter, Devon, United Kingdom

Abstract The North West European Shelf break acts as a barrier to the transport and exchange between the open ocean and the shelf seas. The strong spatial variability of these exchange processes is hard to fully explore using observations, and simulations generally are too coarse to simulate the fine-scale processes over the whole region. In this context, under the FASTNEt program, a new NEMO configuration of the North West European Shelf and Atlantic Margin at 1/60° (∼1.8 km) has been developed, with the objective to better understand and quantify the seasonal and interannual variability of shelf break processes. The capability of this configuration to reproduce the seasonal cycle in SST, the barotropic tide, and fine-resolution temperature profiles is assessed against a basin-scale (1/12°, ∼9 km) configuration and a standard regional configuration (7 km resolution). The seasonal cycle is well reproduced in all configurations though the fine-resolution allows the simulation of smaller scale processes. Time series of temperature at various locations on the shelf show the presence of internal waves with a strong spatiotemporal variability. Spectral analysis of the internal waves reveals peaks at the diurnal, semidiurnal, inertial, and quarter-diurnal bands, which are only realistically reproduced in the new configuration. Tidally induced pycnocline variability is diagnosed in the model and shown to vary with the spring neap cycle with mean displacement amplitudes in excess of 2 m for 30% of the stratified domain. With sufficiently fine resolution, internal tides are shown to be generated at numerous bathymetric features resulting in a complex pycnocline displacement superposition pattern.

1. Introduction

Fine-scale and high-frequency dynamical processes are defining features of the coastal and shelf seas. Examples include boundary currents, internal tides, eddies, coastal-upwelling jets and filaments, tidal straining, and benthic boundary layer processes such as Ekman drains and cascades (see Huthnance, 1995 for a review). This dynamical complexity arises as many of the dominant dynamical scales decrease with reducing water depth (e.g., barotropic and baroclinic Rossby radii; see e.g., Holt et al., 2017). The processes then have complex interactions with tidal phenomena and other bathymetric interactions whose amplitudes and significance generally increase as the water depth decreases. These shallow seas are of substantial societal importance owing to the diverse range of resources and services they provide, and hazards they create for coastal communities. These societal impacts are often mediated by the fine-scale processes. Therefore, understanding how the resources, services, and hazards might change under, for example, large-scale natural and anthropogenic climatic variability requires a detailed understanding of these fine-scale processes. Such understanding can be achieved with a combination of modeling, in situ, and Earth observational studies.

Here we focus on the North-Western (NW) European continental shelf and the adjoining regions of the North-East Atlantic. This shelf broadens northward from Portugal to include the Celtic, Irish and North Seas, and the outer shelves around Ireland and Scotland. We introduce a new fine-resolution model of this region, exploring its properties in the context of small-scale and high-frequency processes as well as new observations from the NERC FASTNEt program. There have been several fine-resolution modeling studies of seas in this region (e.g., Holt & Proctor, 2008; Proctor & James, 1996; Schrum, 1997), but here we introduce a model domain that spans both the shelf seas and open ocean at a scale (1.8 km) that permits motions at the length scale of the first baroclinic Rossby radius on-shelf, resolves the tidal excursion (Polton, 2015) and

many of the fine-scale topographic features that simple do not exist in coarser model configurations. Extending the domain boundary into the open ocean permits an investigation of the across-shelf dynamics at sufficient resolution to capture the important processes, removing complications that may arise when imposing lateral boundary conditions at or near the shelf break.

Coastal seas play a considerable role in the sequestration of atmospheric CO_2 by the oceans (Muller-Karger et al., 2005; Rippeth, 2005), reducing the effects of anthropogenic CO_2 emissions on the global climate. As a result of high levels of phytoplankton production, the NW European continental shelf accounts for almost a third of the North Atlantic Ocean carbon uptake (Frankignoulle & Borges, 2001). This carbon can be exported below the summer thermocline (through mixing and sedimentation) where it is either buried, transported to deep water off shelf or outgassed to the atmosphere following subsequent winter mixing. The former two cases effectively isolate the carbon from the atmospheric system, the latter does not and the balance between these is crucially dependent on the mixing and transport in the shelf sea on seasonal time scales. This shelf-sea carbon pump is in contrast to the deep-ocean carbon pump where the organic material simply has to sink below the permanent thermocline to be isolated from the atmosphere. Hence, to understand the shelf-sea carbon pump, we must first understand the details of the, usually fine-scale, mixing and transport processes a shelf-wide scale.

The highly productive seas of the NW European continental shelf support substantial fishing efforts (Pinnegar et al., 2002) and its ecosystems are therefore vulnerable to direct anthropogenic impacts from the populous, industrialized countries at its margins (e.g., through coastal Eutrophication). This vulnerability is acknowledged in the various policy measures enacted to maintain Good Environmental Status of these seas (e.g., the EU's Marine Strategy Framework Directive). These ecosystem services and issues are mediated by the same fine-scale dynamical processes, e.g., mixing at fronts and subsurface bathymetric banks that support fisheries (Palmer et al., 2013; Sharples et al., 2013) and river plume dynamics controlling the transport of terrestrial material to the wider sea (Hopkins & Polton, 2012; Lenhart et al., 2010).

Here we present an assessment of the capability of the new regional configuration at 1.8 km resolution to reproduce realistic dynamics. We compare with two other NEMO (Nucleus for European Modeling of the Ocean) configurations at lower resolution, in order to better understand the impact of finer resolution, both in the open ocean and on the shelf. The configurations used are 1) a 7 km resolution Atlantic Margin Model (AMM7) configuration, which is the predecessor of AMM60, and 2) a 1/12° basin-scale configuration of the Northern North Atlantic (NNA), used to provide oceanic boundary conditions for AMM60 and AMM7. These configurations are detailed in section 2. A validation of the configurations against observations is made in section 3, to verify that the fine-resolution configuration can reproduce the barotropic tides; seasonal variability in surface temperature and fine-scale depth and variability of the pycnocline depth. The case is made that internal tides are present in the observations, but only adequately resolved in the AMM60. In section 4, the spatial and temporal variability of the internal tides are investigated in AMM60.

2. Model Configurations and Forcing

Here we briefly described the three model configurations used in this study in order of refining resolution: NNA, AMM7, and AMM60. The main parameterization choices are presented in Table 1.

The Northern North Atlantic (NNA) basin configuration is based on an extraction from the NOC 1/12° global ocean general circulation model (Duchez et al., 2014), see Holt et al. (2015, 2017) for further details. It is based on v3.4 of the NEMO ocean model code (Madec, 2008) and spans the North Atlantic from 25°N to 75°N, encompassing the subpolar gyre and a large part of the subtropical gyre (Figure 1). The choice of 25°N allows a south-western boundary condition including the Florida Strait. The NNA configuration adopts the vertical discretisation of its parent grid, 75 z-levels with partial steps allowing robustness at the boundaries, and is generally configured in an identical fashion to the global 1/12° model, apart from the use of lateral boundary conditions, tidal forcing and Generic Length Scale (Umlauf & Burchard, 2003) vertical mixing.

The NNA model uses a split explicit surface pressure gradient calculation with variable volume grid cells, rather than the filtered free surface scheme used in the global model. Lateral diffusion is handled by an isoneutral Laplacian operator for tracers and bi-Laplacian operators for momentum. The initial and boundary conditions for the NNA simulations are derived from the global 1/12° parent simulation. Tracer and dynamic

Table 1
Main Numerical Choices for the Three Configurations Used in the Study

	NNA	AMM7	AMM60
Time step (s)	240	300	60
Horizontal viscosity	Bi-Laplacian (-1.25×10^{10} m^4/s)	Bi-Laplacian (-1×10^{10} m^4/s)	Laplacian (50 m^2/s)
Background vertical viscosity	1.2×10^{-6} m^2/s	0.1×10^{-6} m^2/s	0.1×10^{-6} m^2/s
Bottom friction	Nonlinear, no log-layer (drag coef.: 2.5×10^{-3})	Nonlinear, log-layer (min drag coef.: 10^{-3})	Nonlinear, log-layer (min drag coef.: 2.5×10^{-3})
Advection scheme	TVD	TVD	TVD
GLS scheme	$k-\epsilon$ (Canuto A)	$k-\epsilon$ (Canuto A)	$k-\epsilon$ (Canuto A)
Lateral diffusion of tracers	125 m^2/s	Laplacian along geopotential 50 m^2/s	Smagorinski (factor 0.7)
Vertical coordinates	z coord. with partial steps	s-sigma (Siddorn & Furner, 2013): critical depth = 50 m, rmax = 0.24	s-sigma (Siddorn & Furner, 2013): critical depth = 150 m, rmax = 0.1

variables are interpolated onto the boundary points of the NNA domain using 5 day mean outputs from the global simulation. The tidal harmonic forcing is described below.

The AMM7 configuration is an implementation of the NEMO model (v3.6) of the Atlantic Margin domain covering the NW European continental shelf and adjacent deep ocean and nested within the NNA domain (20°W–13°E, 40°N–65°N; Figure 1). It builds on previous operational AMM7 implementations using NEMO v3.2 (O'Dea et al., 2012) and v3.5 (O'Dea et al., 2017). AMM7 has a horizontal resolution of 1/15° latitude by 1/9° longitude (≈7 km) on a spherical-polar grid and uses 51 hybrid s-sigma-coordinate levels in the vertical. This terrain-following system, with variable vertical resolution, employs the Siddorn and Furner (2013) refinement of constant surface layer thickness. The vertical coordinate definition includes enveloping bathymetry that allows in/out-cropping of sigma layers and prevents excessively steep coordinate surfaces. A critical depth is of 50 m is set up, where there is a transition from pure sigma to stretched coordinate.

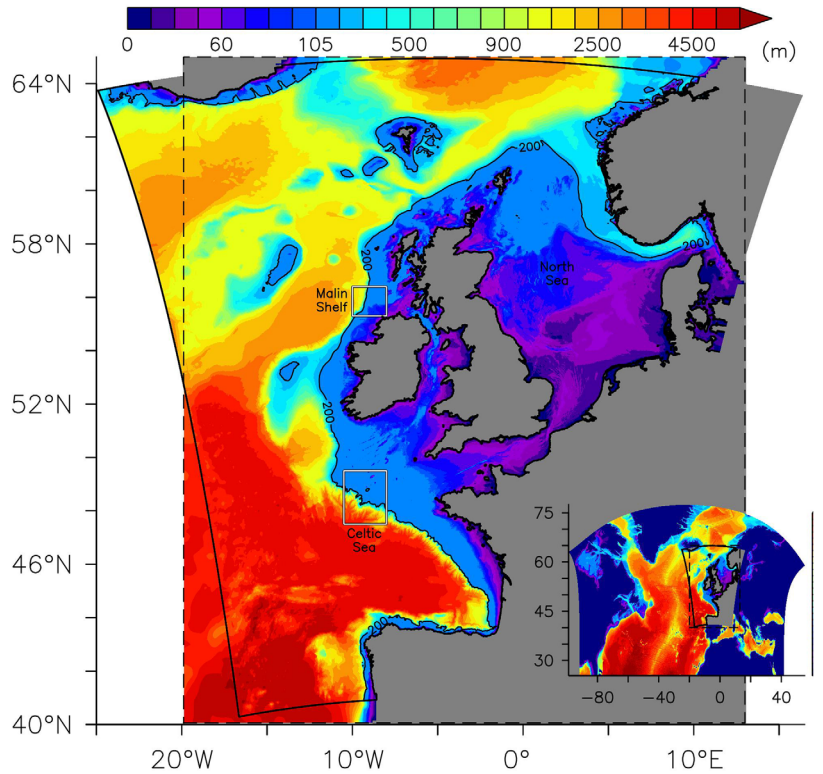

Figure 1. Bathymetry of the AMM60 domain (delimited by the solid black line) plotted over AMM7 domain (delimited by dashed line), in meters. The intensive study regions from the FASTNEt project are highlighted (white squares) and the 200 m isobath which delimits the shelf break is shown. The domain of NNA is shown in the right bottom corner.

Explicit horizontal diffusion is implemented by a Laplacian operator for tracers and Laplacian and bi-Laplacian operators for momentum. The lateral eddy mixing coefficient depends on the local mesh size at each grid point.

The domain of the fine-resolution configuration AMM60 is based on the AMM7 configuration (using NEMO v3.6), spanning from Spain up to Norway, including the Celtic Sea, Irish Sea, North Sea, and a part of the Baltic Sea (Figure 1). The horizontal resolution is 1/60° but an Euler rotation is applied to the spherical-polar grid such that a pseudo equator passes through the domain, resulting in a grid with a regular resolution of approximately 1.8 km both zonally and meridionally. The latitudinal and longitudinal extents are from 40°N to 65°N and from −25°E to 17°E. There are 51 hybrid s-sigma levels in the vertical as in the AMM7 configuration. The parameter choices in AMM60 are similar to those of AMM7. However, as the AMM60 resolves finer scale processes, the lateral mixing is better controlled with a scale-selective diffusion (Smagorinsky, 1963) in combination with a Laplacian operator to explicitly add numerical diffusion in the model and limit the diffusion of the tracer field. The minimum depth of the domain is set to 10 m, with a surface grid box thickness of 1 m. The critical depth is set to 150 m. For further technical detail on this class of model refer to Graham et al. (2017). The bathymetry is derived from General Bathymetric Charts of the Oceans (GEBCO 2014) at 30″ resolution (http://www.bodc.ac.uk/data/online_delivery/gebco/).

The regional simulations are forced at the surface by ERA-interim meteorological forcings (Dee et al., 2011), an atmospheric reanalysis provided by ECMWF (European Centre for Medium-Range Weather Forecasts) that has a spatial resolution of approximately 79 km, covering the period since 1989. The ERA-interim products (wind velocity components at 6 h temporal resolution, air temperature and humidity, radiative fluxes, and precipitation fields, at 3 h resolution) are used to compute the turbulent fluxes and evaporation using the CORE bulk formulation. The NNA simulation is run for the period 1980–2013. The period 1980–2005 is run using the using the The DRAKKAR Forcing Set (DFS; Brodeau et al., 2010) for surface boundary conditions; a blend of the CORE data (Large & Yeager, 2004) and ECMWF reanalysis data (Uppala et al., 2005). The period 2005–2013 is run using ERA-interim surface forcing to be consistent with AMM60 and AMM7.

The oceanic forcing is prescribed through the Flow Relaxation Scheme (FRS) for the tracers and the Flather radiation condition for the depth-mean transports (Flather, 1976). A barotropic solution (sea surface height and barotropic velocities) and the tracers (T, S) are prescribed along the boundaries. Along the open boundaries in AMM7 and AMM60, a relaxation zone of 10 grid points is used where the FRS is applied. This enhances model stability by preventing spurious reflection of outgoing signals from the boundary (Madec, 2008). Tidal processes are implemented using both gravitational forcing and as prescribed velocities and elevations at the oceanic boundaries. The boundary tidal forcing consists of nine leading constituents (Q1, O1, P1, K1, M2, S2, N2, K2, and M4) and was generated using the Oregon State University Inverse Tidal Model TPXO7.2, which assimilates altimetry into a global shallow-water model at 1/4° resolution (Egbert & Bennet, 1994; Egbert & Erofeeva, 2002).

The coastal NW European Shelf also has a significant number of coastal rivers to consider. Freshwater fluxes are implemented using daily discharge data for 322 rivers synthesized from the Global River Discharge Data Base (Vörösmarty et al., 2000) and from data prepared by the Centre for Ecology and Hydrology. These synthesized data cover the period 1950–2005, using gauged discharges where available and filling gaps with a mean annual cycle for each river. Initial conditions for temperature, salinity, and sea surface height for both the regional configurations are derived from a 5 day mean output from the NNA configuration at the date at the beginning of the intercomparison run (5 January 2010). Both AMM7 and AMM60 are run up to November 2013, in order to provide numerical support to the FASTNEt cruises.

3. Assessment of the Configurations

3.1. Tidal Validation

The barotropic tides are a dominant feature of the NW European Shelf Seas. It is therefore necessary to evaluate the ability of the configurations to reproduce the amplitude and phase of tidal elevations and currents. A harmonic analysis of the tide is made on 1 year of tide-only forced simulation with constant temperature and salinity, for the three configurations. Comparisons are made for seven major constituents using tide-gauge and current meter data from the British Oceanographic Data Centre (BODC).

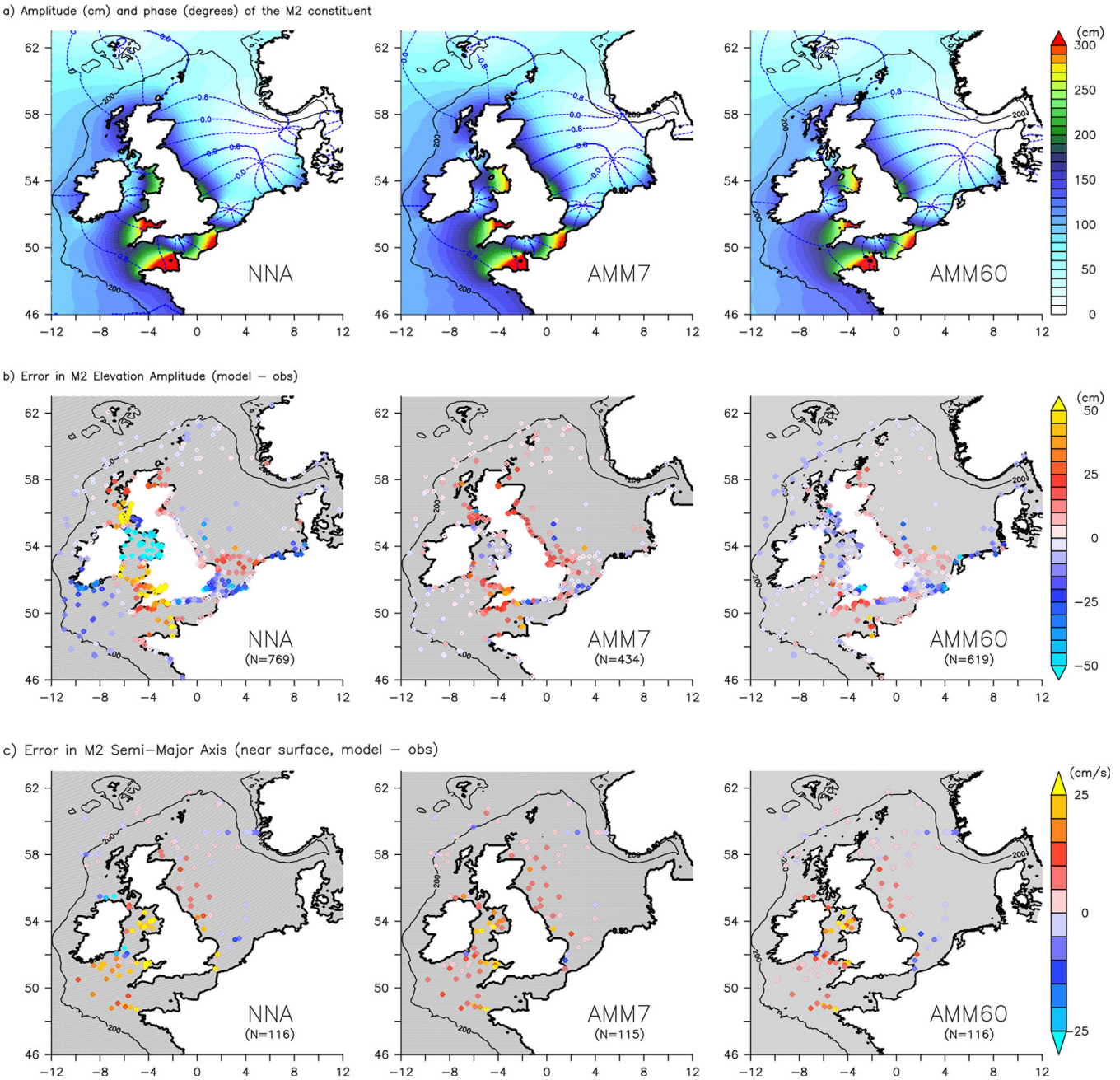

Figure 2. (a) Cotidal chart of M2 for NNA, AMM7, and AMM60, from left to right, and distribution of error (model – observations) of (b) M2 amplitude and (c) M2 semimajor axis from a comparison against tide gauges and current meters. The 200 m isobath is in black.

Qualitatively, the cotidal chart of the M2 constituent, which is the most dominant over the whole region, is in good agreement with previous studies (see e.g., Howarth & Pugh, 1983; Kwong et al., 1997) for all configurations. The location of the amphidromes in the North Sea and Irish Sea are accurate and the cotidal chart (Figure 2a) shows similar amplitudes and phases. An important exception is where the degenerate amphidrome on the south coast of Norway moves erroneously offshore in the NNA configuration. This most likely reflects the different frictional characteristics and bottom boundary layer resolution in this *z* coordinate configuration. The spatial distribution of the M2 differences between the modeled and observed data is shown in Figures 2b and 2c. Figure 2b shows the (model-observed) M2 amplitude. It is noteworthy that the AMM7 simulation consistently overestimates the tidal elevations around the coastline, whereas the AMM60 has a less biased coastal amplitude. Both AMM7 and AMM60 perform well in deep water. The NNA exhibits less

Table 2
RMS Error and Mean Error (Model Minus Observation) of Tidal Current and Amplitude

	Elevation (cm)			Current (cm/s)		
Constituent	RMSE	Mean	N	RMSE	Mean	N
NNA (tide only)						
Q1	0.778	−0.269	693			
O1	1.248	−0.322	764	0.838	0.340	114
K1	1.622	−0.839	758	0.956	0.015	114
N2	6.220	−0.690	766	3.582	1.189	112
M2	33.588	1.005	769	21.805	9.774	116
S2	9.449	−0.710	771	5.916	3.025	116
M4	5.990	0.602	709	1.798	0.343	113
AMM7 (tide only)						
Q1	0.923	−0.462	388			
O1	1.124	−0.463	427	0.790	0.182	114
K1	1.294	−0.205	428	0.980	0.219	114
N2	5.344	−3.358	432	2.319	−0.400	112
M2	13.954	6.489	434	10.800	6.864	115
S2	5.012	2.234	434	3.942	2.534	115
M4	4.591	1.125	392	1.354	0.072	115
AMM60 (tide only)						
Q1	0.843	−0.366	565			
O1	1.403	−0.905	615	1.043	0.083	114
K1	1.551	−0.913	613	0.921	−0.007	114
N2	3.402	0.215	616	2.689	0.894	112
M2	16.018	−6.571	619	10.027	4.543	116
S2	6.430	−1.633	619	3.569	1.714	116
M4	5.915	0.229	571	1.266	−0.142	113
AMM60						
Q1	0.815	−0.301	565			
O1	1.178	−0.488	615	0.880	0.194	114
K1	1.410	−0.594	614	0.912	0.112	114
N2	3.643	0.663	616	2.798	1.047	112
M2	14.476	−2.282	619	11.060	5.717	116
S2	6.546	−0.705	669	3.800	2.047	116
M4	6.244	0.820	570	1.208	−0.080	113

Note. AMM60, AMM7, and NNA models comparison against harmonic analyses from historical current meter and tide-gauge data around the shelf. The number of valid measurements N is shown for each data.

skill for this diagnostic in particular in the neighborhood of the amphidromes in Irish Sea off the SE coast of the UK. Figure 2c shows the (model-observed) semimajor axis. The simulated fields exhibit a positive bias in the AMM60 and AMM7 configurations, with a notable exception in the Thames mouth where the shallow estuary will not be well resolved.

In order to make a quantitative assessment of the tides, comparisons against tide-gauge data located on the shelf, and processed by BODC, have been made. These results can be compared with other studies which have used the same data set (Holt et al., 2005; Maraldi et al., 2013; O'Dea et al., 2012). Since many of the gauged data are from secluded harbors their locations, when interpolated onto the model grid, are located within land grid boxes. As a consequence the number of data points in the tidal validation varies between the configurations, which each resolve the coastline at different resolutions. The current meter data set and the code used for this analysis have been made available under a CECILL license at https://github.com/Karen-Guihou/tidal_analysis.

Table 2 shows the RMSE $\sqrt{\frac{\sum (mod-obs)^2}{N}}$ and mean error $\frac{\sum (mod-obs)}{N}$ for both the tidal harmonic elevation amplitude and the semimajor axis of the barotropic tidal velocity, for the leading constituents. The M2 elevation results here have somewhat higher RMSE than the operational AMM7 implementations of 10.3 cm (O'Dea et al 2012) and 11.4 cm (O'Dea et al 2017), most likely reflecting differences in bathymetry and forcing. Interestingly, the NNA gives notably higher RMSE (although not biases) for M2 tides. This might

be due to this model tidal boundary conditions being imposed far from the shelf region. It is also missing two important dynamical features implicitly included in the observationally constrained boundary conditions of the smaller area models: self-attraction and loading, and internal wave drag (Arbic et al., 2010).

The cotidal chart and spatial variations of amplitude and currents are of the same order between this tide-only simulation and the realistic run used further in this study (figure not shown), with RMSE and mean error of both simulations of the same order (Table 2).

3.2. Seasonal Variability of Surface Temperature

Given the readily available data, sea surface temperature (SST) is a natural starting point for validating the hydrography. Here we present a configuration intercomparison and assessment of the SST seasonal cycle. Figure 3 shows the mean surface temperature fields for winter and summer 2012 from satellite data, and difference of mean seasonal SST between model and satellite. The Odyssea satellite products, provided by the Copernicus service (http://marine.copernicus.eu), offers daily gap-free L4 maps of surface temperature on the NW European Shelf Sea, with a 0.02° × 0.02° horizontal resolution (1/50°) since September 2010. This SST assessment is performed after 3 years of model spin-up.

Consistent across the data sets, in winter the open ocean is warmer than the shelf, with mean temperatures up to 14.5°C in the southern part of the domain. This on and off shelf temperature difference arises as open ocean winter mixed layer depth exceeds the shelf bathymetric depth and so has a larger thermal reservoir. The open ocean waters mix at the shelf break with the colder Celtic Sea shelf water (up to 10°C) leaving a warmer thermal fingerprint along the shelf break in the Celtic Sea. Off shelf the warmer subtropical gyre Atlantic waters are advected northward along the shelf break as far as the Norwegian Trench. In summer, the shelf waters stratify and exhibit the same latitudinal signature as the offshore waters.

All configurations reproduce these broad scale seasonal patterns. The offshore surface temperature is slightly too warm in summer, but not biased in winter. NNA overestimates the intrusion of the cold waters from the north of the domain in the Greenland Sea (not shown) all year long, and the same bias exists in the global 1/12° model used at its boundaries. This cold water bias is imposed on both regional

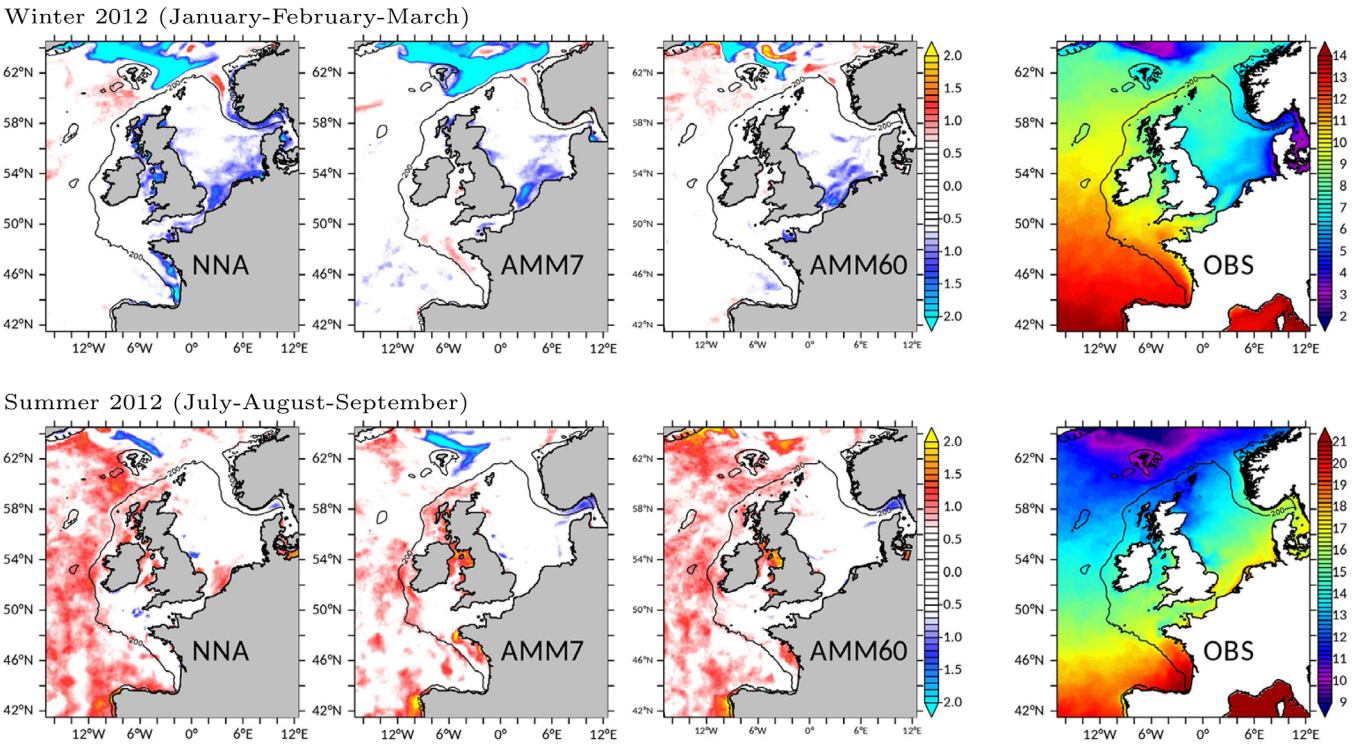

Figure 3. Difference of mean seasonal SST for (top) winter 2012 (January–February–March) and (bottom) summer 2012 (July–August–September). From left to right: mean difference (model – obs) for NNA, AMM7, AMM60, and Odyssea satellite SST. The shelf delimitation (defined as the 200 m isobath) is in black.

configurations through the northern boundary conditions. It is interesting to note that in AMM60 and consistent with observations, these cold waters do not enter the Faroe-Shetland channel (~60°N, 6°W), suggesting the complex currents in this region are better represented in AMM60.

3.3. Thermocline Depth

In a seasonally stratified shelf sea, the vertical structure is characterized by a surface wind-mixed boundary layer over a bottom tidally mixed benthic boundary layer. The mixing of this quasi two-layer system is broadly controlled by wind and tidal mixing from the surface and bed, and by processes associated with internal waves at the interface. The depth of this interface, where the stratification is elevated, and the state properties of the surface and bottom layers must be reproduced accurately by the models in order to achieve realistic levels of bulk mixing. Here we make direct use of the moorings from the FASTNEt program. Observational campaigns to the Celtic Sea (June 2012) and the Malin Shelf (July 2013) were undertaken (Inall & the FASTNEt Team, 2012, 2013). Long-term and short-term moorings were deployed across the outer shelf and shelf break region for multiweeks durations (Stephenson et al., 2015; Vlasenko et al., 2014). The mooring data were augmented by an extensive campaign of glider measurements (Palmer et al., 2015), drifter release experiments (Porter et al., 2016), as well as traditional ship based measurements. Here we use time series of temperature from 5 of the moorings to assess the skill in simulating the depth of the thermocline across the model configurations. Since the depth resolution of salinity sampling was not as high for temperature, observational analysis of the stratification is conducted in temperature only, and so the thermocline depth is computed instead of a pycnocline depth. For comparison, observations and models have been hourly averaged and interpolated on the same vertical grid.

We define the depth of the thermocline, δ_T, as a normalized first moment of stratification (i.e., a depth-weighted depth of stratification):

$$\delta_T = \frac{m_1}{m_0}, \tag{1}$$

where

$$m_n = \int_{-H}^{0} z^n \frac{\partial T}{\partial z}\, dz \tag{2}$$

and depth-mean thermocline is given as

$$\bar{T}(t) = \frac{m_0}{H}. \tag{3}$$

Then, applying the chain rule:

$$\delta_T(t) = H\frac{T_{bed}(t) - \bar{T}(t)}{T_{top}(t) - T_{bed}(t)}. \tag{4}$$

In the limit of a two-layer vertical density structure, the depth of the thermocline is exactly represented by δ_T, where H is the depth of the water column (here limited to the shallower of either the sea bed or 200 m), $T_{bed}(t)$ and $T_{top}(t)$ are the surface and bed temperatures at a given time, and $\bar{T}(t)$ the depth averaged temperature. Temporal variations in H are small relative to the error in the two-layer approximation and are therefore not considered further.

On the Malin Shelf, the SE mooring can be exploited to assess the variability of the on-shelf thermocline depth (Figure 4). A two-layer system is well established, until the appearance of a third layer from the 15 June, associated with a warming of the surface waters. The temperature varies from 11°C at the bottom, to 12.8°C at the surface on the 3 June, with a maximum at 14°C at the surface by the end of the measurement period. The thermocline depth is steady with a mean depth around 40 m. All the configurations reproduce accurate bottom temperatures and thermocline depth. However, the warming of the surface layer in the second part of the time series is consistently biased, both in terms of timing and intensity.

In the Celtic Sea, moorings were deployed in June 2012 at four locations across the shelf (Figure 5). St1 is located on the shelf slope, where depth is 688 m. St2 is at the edge of the shelf break, delimited by the 200 m isobath. Both St4 and St5 are on the shelf, where depth is less than 200 m. St1, St2, and St4 are

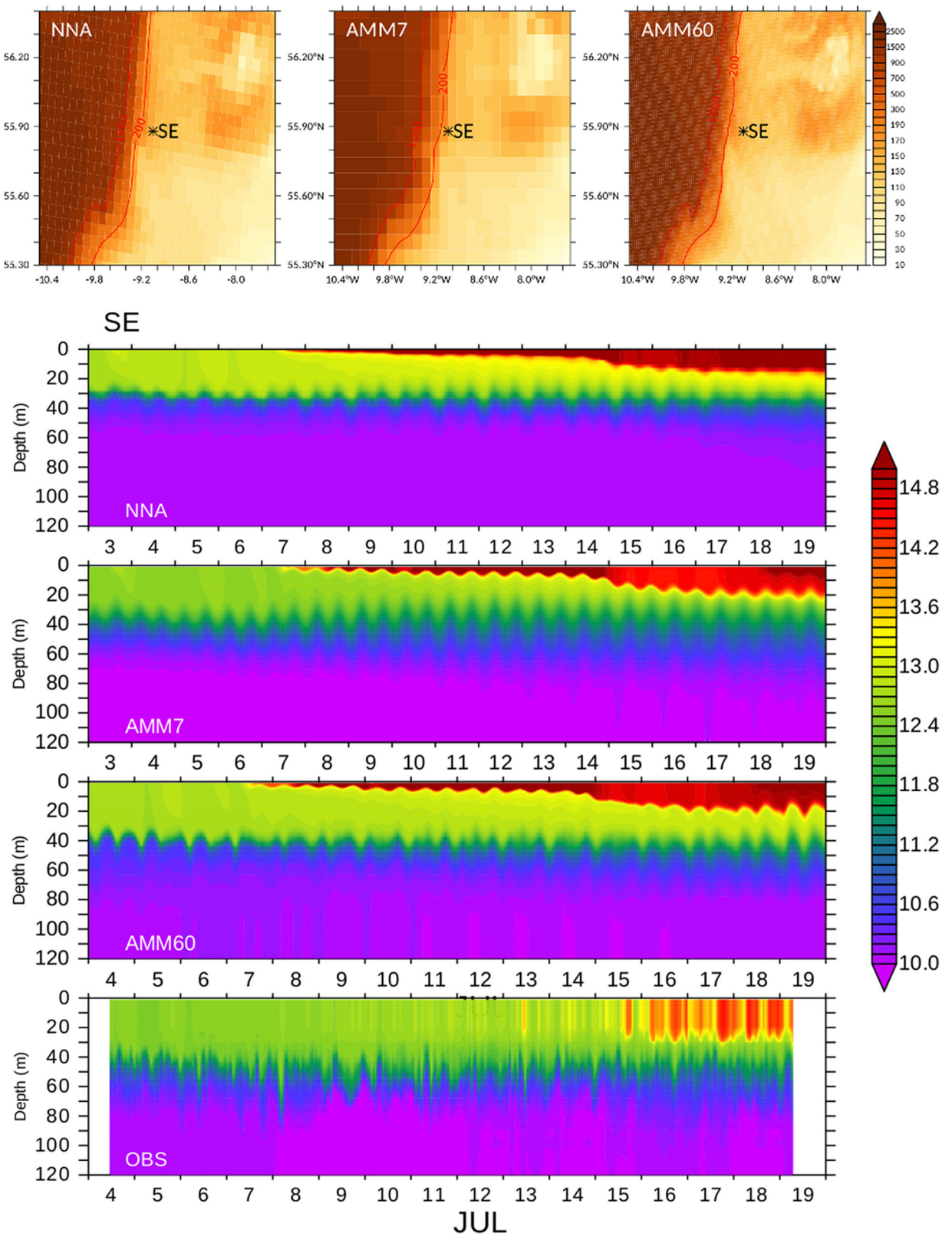

Figure 4. Time series of hourly temperature at SE mooring location on the Malin Shelf, in July 2013. (top) The bathymetry of the configurations and location of SE is shown. (bottom) Time series of temperature for NNA, AMM7, AMM60, and observations (top to bottom) at SE station

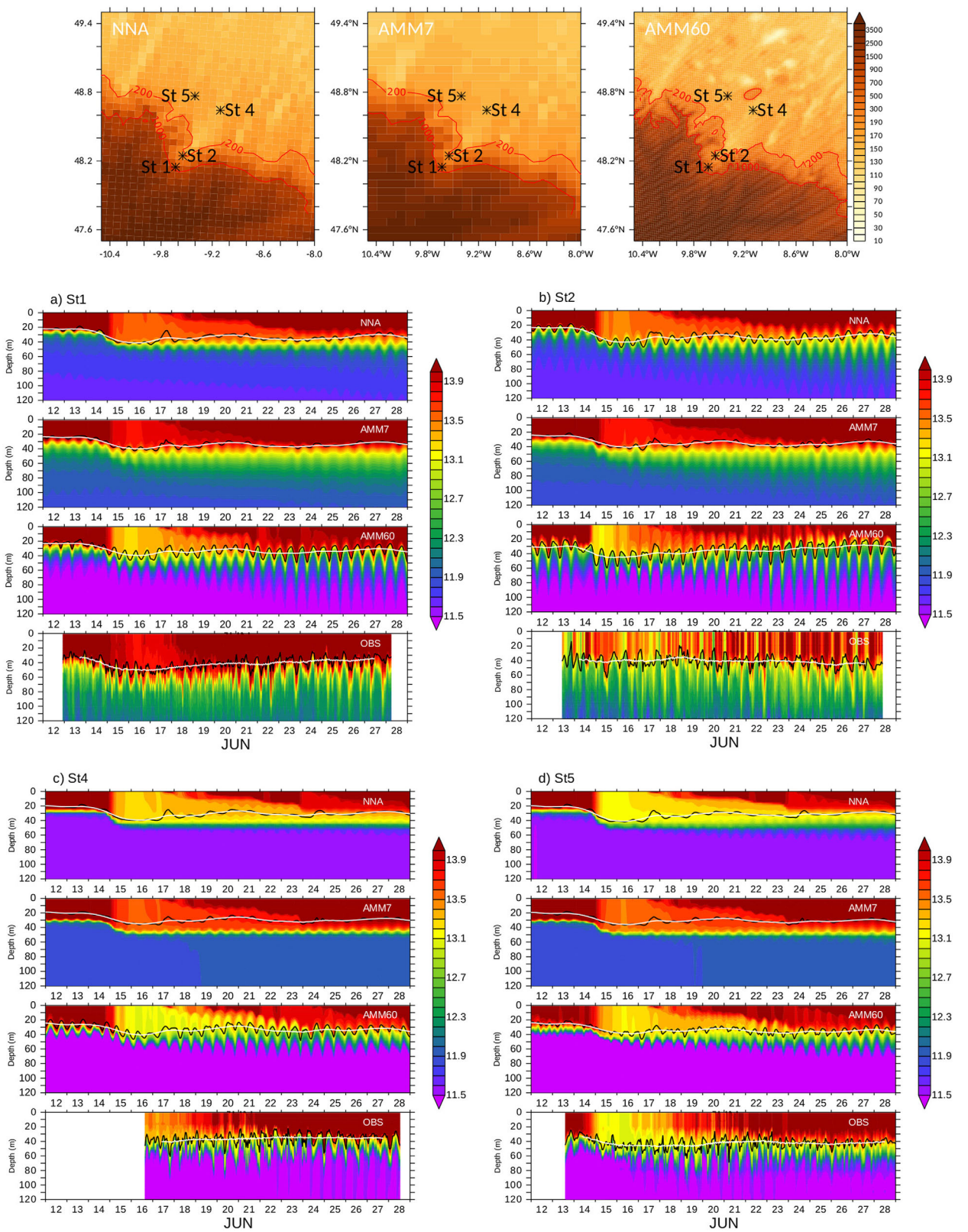

Figure 5. Time series of hourly temperature at four different mooring locations on the Celtic Sea, in June 2012. (top) The bathymetry of the three configurations and the locations of the moorings is shown. The other figures represent time series of temperature for NNA, AMM7, AMM60, and observations (top to bottom) for St1, St2, St4, and St5. The thermocline depth δ_T is shown (black line), also with the tides removed using a DoodsonX0 filter, $\langle \delta_T \rangle$ (white).

positioned in an across-shelf transect line, in order to monitor the cross-shelf transport and the propagation of internal tides across the shelf break. Similar to the Malin Shelf mooring data, the temperature time series show a well-established two-layer system (Figure 5).

The thermocline depth δ_T is represented by the black line in Figure 5. In order to analyze the slowly varying thermocline displacement (independent from tides), a DoodsonX0 filter is applied to hourly δ_T fields to isolate the diurnal and higher tidal species (Doodson, 1921; Pugh, 1996). Distinct from surface height data processing, where the longest filter is sought according to the frequency of missing data occurrences, wave properties of internal tides are continually modified by the evolving stratification. This makes the DoodsonX0 filter, with a relatively short filter window of 39 h, ideal for these purposes. The white line in Figure 5 corresponds to the signal filtered for tides with the DoodsonX0 filter $\langle\delta_T\rangle = \mathrm{DoodsonX0}(\delta_T)$ (IOC, 1985).

The thermocline depth at the Celtic Sea shelf break varies between 40 and 60 m, with colder waters at the bottom (12.5°C at the shelf break, and 11.5°C on the shelf), while surface temperatures vary from 13 to 14°C. There is a cooling of the surface layer and deepening of the thermocline on the 15 June, correlated with a storm event, followed by a progressive return to a shallower warmer surface layer (Hopkins et al., 2014; Stephenson et al., 2015). This is observed at the four locations, but one can notice more mixing of the bottom layer at the shelf break (St1 and St2). The three configurations simulate similar thermocline depths, in good agreement with the observations at all locations. The deepening and cooling of the surface layer during the storm event at the Celtic Sea shelf break is well reproduced. However, the bottom temperatures are not accurately reproduced at the shelf break (St1 and St2) with all three configurations being too cold in the lower layer. The lower layer temperature in AMM7 is closest to the observations but the thermocline variance is more realistic in AMM60. In reality, all configurations will under represent the vertical mixing at the shelf break as a result of the locally generated nonhydrostatic internal waves, which cannot be resolved in this class of hydrostatic models, even though the vertical resolution might actually introduce quite some damping into the process. On the shelf (St4 and St5), it is the fine-resolution configuration which has the more realistic results, with accurate bottom temperature, whereas the coarser configurations are too warm.

3.4. Internal Waves

In order to analyze the tidal contribution to the thermocline depth variability, $\tilde{\delta_T}$, the tidally varying thermocline depth is defined as

$$\tilde{\delta_T} = \delta_T - \langle\delta_T\rangle. \tag{5}$$

Though the tidally filtered thermocline depth $\langle\delta_T\rangle$ is well reproduced and similar across all the configurations, a major difference exists between the reproduction of the hourly thermocline variability $\tilde{\delta_T}$ (Figure 5).

Internal tides are evident at the thermocline, with amplitudes reaching almost 29 m at St5 (Table 3). Evidently, the finest scale horizontal grid (AMM60) best resolves these high-frequency processes. The mean amplitude of the observed thermocline vertical displacement ranges from 5 to 6 m, with similar values in AMM60 at the shelf break. This amplitude is underestimated on the shelf by AMM60, but the coarser NNA and AMM7 produce smaller amplitudes (1–3 m) at all locations.

The use of sigma-coordinates in the regional configurations allow a finer vertical resolution at surface and subsurface than the *z* coordinates in the basin-scale configuration (Figure 6). This is particularly true on the shelf (e.g., at St4 and St5 locations), where the vertical resolution at the thermocline depth (40–60 m) is almost twice finer than in NNA: between 3 and 4 m of resolution for the regional configurations against 6–8 m in NNA. Such vertical grid allow the resolution of the internal waves, which have a mean amplitude of 5 m (Table 2), with maximum amplitude up to 28 m, that is four to five grid cells. Oscillations smaller than 3 m cannot be resolved.

A fast Fourier transform spectral analysis of the thermocline depth, δ_T, is used to identify the dominant frequencies. A Welch filter (Welch, 1967; with 192 h segments) and a Hanning window (with 50% overlap) are used to identify the dominant spectral peaks. The method is applied to the simulations and observations at the four moorings in the Celtic Sea (Figure 5) and presented in Figure 7.

The observations show peaks at the diurnal, semidiurnal, inertial, and quarter-diurnal bands. At all locations the semidiurnal band is the most dominant.

Table 3
Mean and Maximum Amplitude of $|\tilde{\delta}_T|$ in Meters, at the Four Moorings in the Celtic Sea, for the Three Configurations and the Observations, During the Measurement Period

	St1 mean (max)	St2 mean (max)	St4 mean (max)	St5 mean (max)
NNA	1.60 (9.78)	3.23 (10.44)	1.27 (7.94)	1.22 (7.34)
AMM7	1.42 (7.89)	1.58 (7.80)	1.11 (5.55)	1.06 (5.70)
AMM60	4.32 (14.78)	6.12 (18.83)	3.67 (12.53)	2.52 (9.14)
Obs	4.95 (18.25)	5.98 (21.14)	5.61 (21.50)	4.84 (28.94)

Snapshots of the pycnocline depth (Figure 9a) highlight that the wave field exhibits a complex superposition pattern, which varies over short spatial scales relative to the mooring separation scales. Consequently, there is no evident dependence of the variance amplitude on large-scale factors, such as proximity to the shelf break. Instead the amplitude of the wave field, at distinct mooring locations, is more strongly constrained by local factors. For example, the local proximity to wave-generating bathymetric features. The signal at St1 is more energetic than at the other locations, but as shown Table 3, the maximum amplitude of the waves is smaller than at the other locations. The observations variously show energy in the diurnal and M4 bands, again owing to the complexity of the superposition field it is not possible to attribute causes to these spatial variations. All the model configurations exhibit a similar diurnal response at all moorings, which match the observations. AMM7 consistently underestimates the semidiurnal response with a very weak signal. NNA similarly does not capture the semidiurnal signal except at St2, which is on the shelf break, where the energy conversion from barotropic to baroclinic tides is strong due to steep topography (Baines, 1982). Notably, the AMM60 is the only configuration to qualitatively match the observational semidiurnal response, with an amplitude that both overestimates and underestimates the observations. We observe also a gap of energy at 6.65 h, in the observations and AMM60, which may correspond to the nonlinear interaction between the inertial frequency and the M2 tide (Xing & Davies, 2002). This spectral analysis demonstrates that the variations in thermocline depth exhibits clear frequency banding that are best captured by the dominant tidal harmonic bands. On the shelf the semidiurnal band is characterized by propagating internal tides with a wavelength in the range 12–25 km. By way of demonstration, the two-layer fluid dispersion relationship can be solved to infer the wavelength of the semidiurnal features:

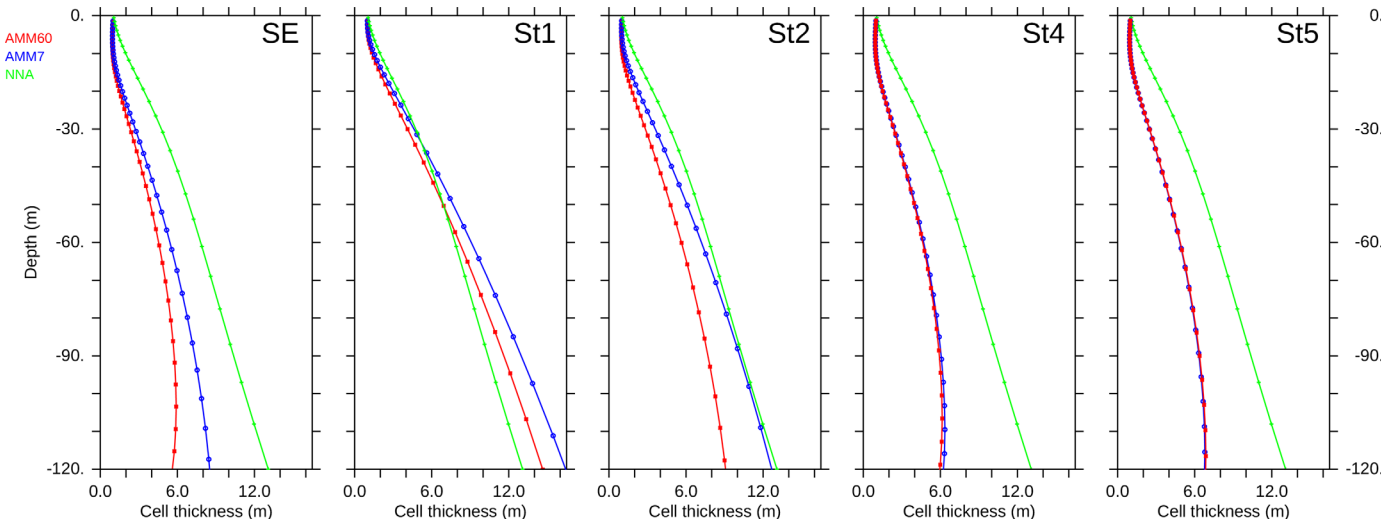

Figure 6. Vertical resolution of the configurations at mooring location, on the Celtic Sea and Malin Shelf. From left to right: SE, St1, St2, St4, and St5 for AMM60 (red), AMM7 (blue), and NNA (green).

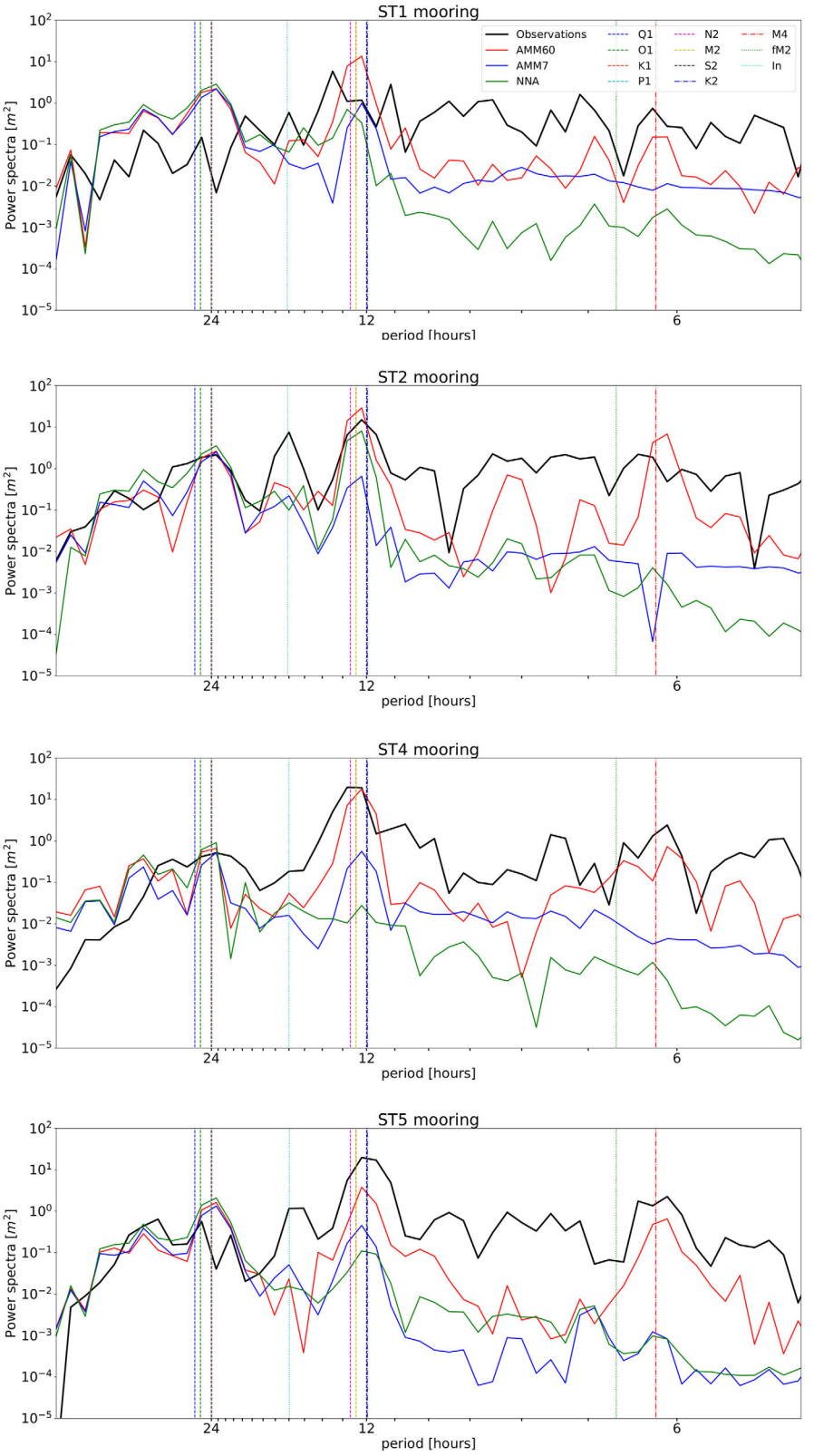

Figure 7. Power spectra of the thermocline variability at the Celtic moorings locations St1, St2, St4, and St5 (top to bottom) for the three configurations and the observations.

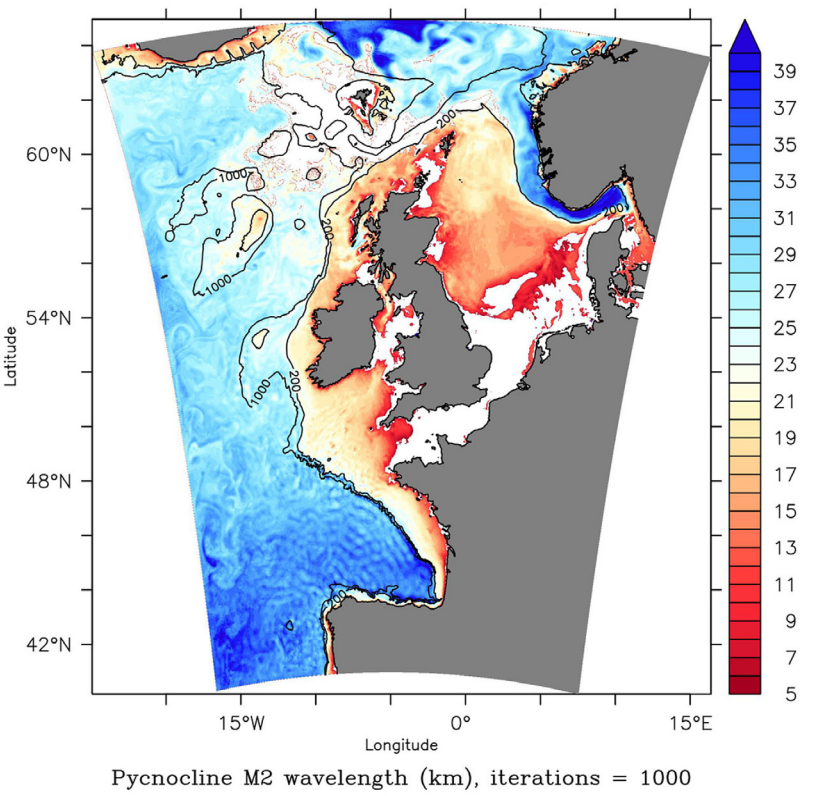

Figure 8. Figure showing the wavelength (km) for an interfacial tide at the M2 frequency, from a snapshot on 21 July 2012. Regions where the bulk stratification was weaker than 3×10^{-3} kg m^{-4} are masked in white.

$$\Omega_{M2}^2(k)=\frac{gk(\rho_{bot}-\rho_{top})}{\rho\coth(kh_{bot})+\rho_{top}\coth(kh_{top})} \tag{6}$$

for wave number k, layer densities ρ_{top} and ρ_{bot}, layer thicknesses h_{top} and h_{bot}, $g=10\,\mathrm{m\,s^{-1}}$, $\Omega_{M2}=2\pi/12.4$ h. Equation (6) is solved iteratively for wave number and shown as a wavelength, $2\pi/k$ (Figure 8). The mean stratification is shown in Figure 9d.

Both the 7 km AMM7 and 1/12° (~9 km) NNA are too coarse to adequately resolve the propagation properties of these features. Therefore, only the 1.8 km AMM60 configuration has fine enough lateral resolution to reproduce: (i) propagating waves of these length scales that are generated at major features such as the shelf break and (ii) the small-scale bathymetric features necessary for on-shelf generation of these internal tides (see Figure 5).

4. Spatial and Temporal Variability of the Internal Tides

Given that (i) the diagnostic δ_T captures the variability in the thermocline depth (under the assumption that the fluid can be approximated as a two-layer fluid) and (ii) the observed thermocline depth variability is captured well, at harmonic frequencies, by only the fine-scale AMM60 model, we proceed to investigate the pycnocline depth, δ, variability across the whole AMM60 model domain, at tidal frequencies.

A spatial snapshot of $\tilde{\delta}$ (Figure 9e) shows a complex superposition pattern of internal tides in the Celtic Sea. This interference pattern is evidently locked to the bathymetry and presents compelling evidence that the internal tide field is generated over many small-scale bathymetric features rather than just at the shelf break and at a few isolated feature in the shelf sea. Further north (e.g., on the Malin Shelf; Figure 9f) where the shelf is narrower and the slope smoother, the internal tides pattern is less complex and localized to larger scale bathymetric features including, but not limited to, the shelf break. The propagation pattern is different in the Northern Sea (Figure 9a), where the shelf waters mix with the fresher waters from the Baltic Sea. The

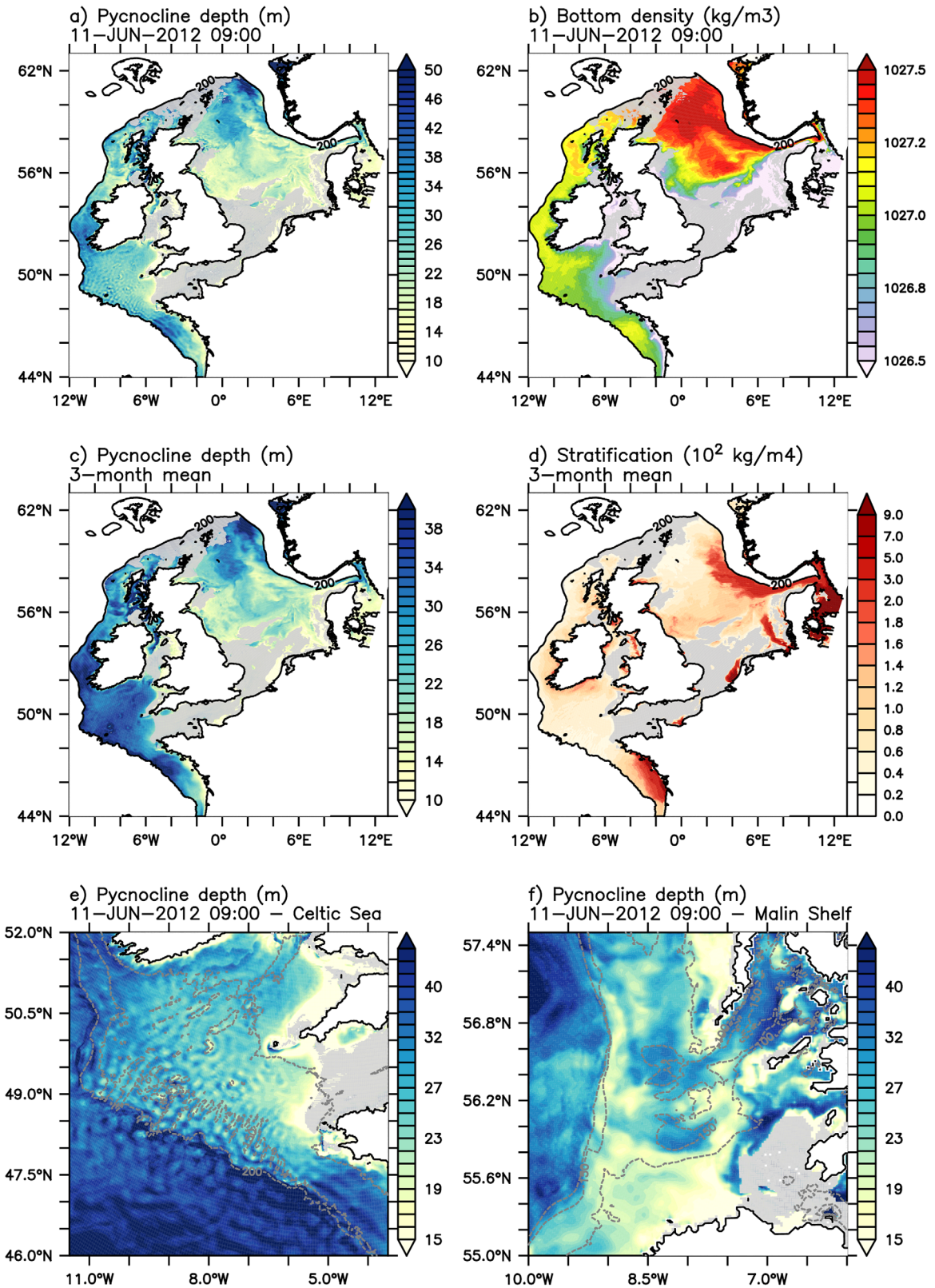

Figure 9. (top) (a) Pycnocline depth and (b) bottom density for the 11 June 2012 at 9 A.M. (hourly mean), as seen by AMM60. The bottom density is taken as the bed density on the shelf and the 200 m deep density in the open ocean. Regions where the bulk stratification was weaker than 3×10^{-3} kg/m^4 are masked in grey. (middle) (c) Mean over 3 months of the pycnocline depth and (d) mean top to bottom stratification, $(\rho_{top}-\rho_{bed})/H$, on the shelf. (bottom) Same as Figure 9a but zoomed on the (e) Celtic Sea and (f) Malin Shelf.

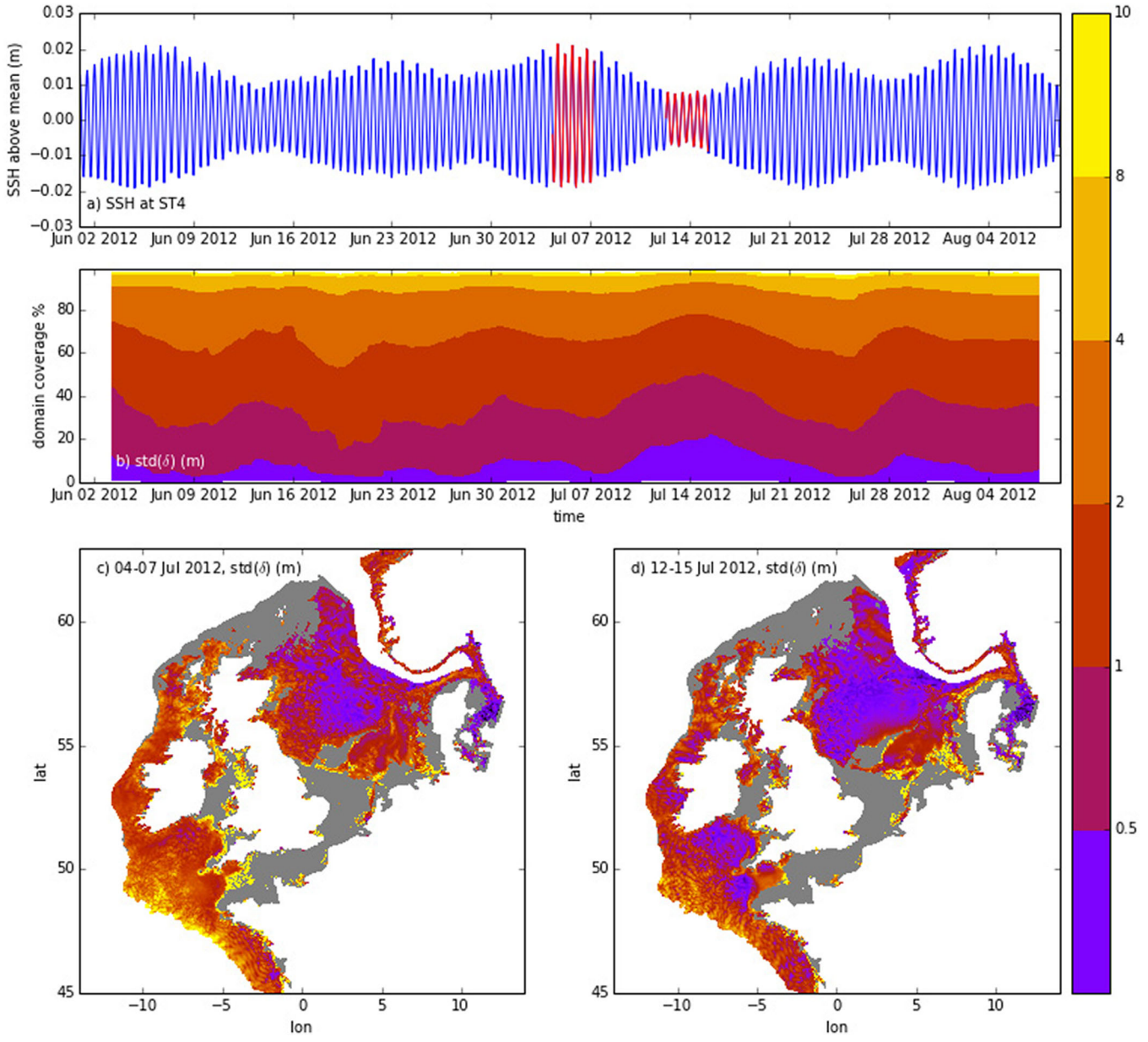

Figure 10. The tidal oscillations in pycnocline depth vary with the spring neap cycle. (a) simulated SSH at St4, characterizing the phase of the spring neap cycle. Red periods correspond to analysis windows for (c) and (d). (b) The domain wide pycnocline depth tidal standard deviation, sorted by magnitude and plotted as varying in time. (c, d) Analysis snapshots of pycnocline depth tidal standard deviation (computed over 3 day windows) during (c) spring and (d) neap phases, with corresponding time windows highlighted in red in Figure 10a. Regions where the bulk stratification was weaker than 3×10^{-3} kg/m^4 are masked in grey.

stratification in the Channel, southern North Sea and northern shelf boundary waters is too weak to resolve internal tides and are masked in Figure 9. Generally, the mean pycnocline depth (averaged over 3 months, Figure 9c) is deepest at the shelf break and shoals on shelf, into shallower waters.

To identify the internal tide activity within the model, the standard deviation of the tidal fluctuations in pycnocline depth is computed. While numerous moorings have been deployed across the seasonally stratified shelf, this quantity is unknown on a shelf-wide scale. Furthermore, this first attempt to compute the internal tide variability highlights a physical process that is either entirely missing or only partially resolved in coarser resolution models. Here we provide a first look at the spatial and temporal tidal variability of the pycnocline depth; a comprehensive internal tide energy budget is the subject of on-going work.

The standard deviation of $\tilde{\delta}$ is computed over a moving 3 × 24 h window. This is a compromise to avoid aliasing from the time evolving spring neap cycle while retaining sufficient data (∼6 semidiurnal cycles) to isolate a clear signal. This represents a conservative estimate of the tidal variability in the pycnocline displacements and is formally defined as

$$\mathrm{std}(\tilde{\delta}(t)) = \sqrt{\frac{1}{72}\sum_{t-36h}^{t+36h}\left(\tilde{\delta}(t) - \frac{1}{72}\sum_{t-36h}^{t+36h}\tilde{\delta}(t)\right)^2}. \quad (7)$$

The std($\tilde{\delta}$) varies in space and time (Figure 10). Typical snapshots during seasonal stratification (spring tide: Figure 10c; neap tide: Figure 10d) demonstrate the standard deviation is generally lower than the domain average in the North Sea and generally higher in the Celtic Sea, increasing toward the south western bounding isobath. At the edge of weakly stratified (masked) fluid the standard deviation increases, though this does not represent increased wave energy levels because it corresponds to reduced stratification. Here the stratification mask is applied over the whole record to preserve the analysis domain size for stratified fluid. As in Figure 9a, there is a lot of fine-scale structure confirming that the features seen in the pycnocline depth snapshot are not stationary features but are oscillatory. This is consistent with the nonhydrostatic simulations of internal tide generation over rough topography in the Celtic Sea (Vlasenko et al., 2013, 2014).

While nonhydrostatic studies (e.g., Vlasenko et al., 2013, 2014) have previously captured spatial variability of internal wave activity over smaller regions and short time ranges, the computational efficiency of the hydrostatic approximation permits a larger time step and therefore longer time integration (or spatial domain). An investigation of the 2 month period during the summer of 2012 (chosen to overlap with the FASTNEt mooring campaign) demonstrates that the std($\tilde{\delta}$) varies with the spring neap cycle. At each hour, the spatially varying, 3 day windowed, std($\tilde{\delta}$) is sorted by amplitude and plotted against the fractional area of the unmasked domain for which std($\tilde{\delta}$) is the maximum value (Figure 10b). That is averaging over time, the std($\tilde{\delta}$) < 1 m for ∼30% and std($\tilde{\delta}$) > 2 m for ∼30% of the unmasked domain. Figure 10b shows the std increases following neap tides (e.g., 16 June, 30 June, 14 June, and 28 June) and similarly decreases following spring tides. Figures 10c and 10d show the spatial differences between representative spring and neap phases, with the changes being of the order a factor of 2 and most marked in the Celtic and North Seas. It clearly shows the region of low variance in the North Sea and Celtic Sea expanding at neap tides, but other areas showing less variation.

5. Discussion and Conclusion

A basin-scale configuration and two regional NEMO ocean model configurations, focusing on the NW European Shelf, are assessed in order to evaluate the improvement brought to the reproduction of high-frequency processes by horizontal resolution at the kilometric scale. For the NW European Shelf domain of interest the regional configurations take their boundary conditions from the basin-scale configuration and all three configurations use the same forcing data set. The coarse regional simulation, AMM7, has already been validated (O'Dea et al., 2012) and a variant is used operationally by the UK Met Office. This is the first attempt to develop a fine-resolution configuration spanning a comparable domain, and therefore including the shelf break. While other fine-scale studies have investigated internal waves they are typical short integrations and small domains (Vlasenko et al., 2013, 2014). Here by retaining the hydrostatic balance simplification we integrate multiyear simulations over a large domain. Previous fine-resolution configurations from the POLCOMS model were bounded by the 200 m shelf break isobath (Holt & Proctor, 2008) such that the shelf break processes were imposed as boundary conditions. Such fine-resolution configurations are a challenge, both in terms of cost and stability of the model. Fine-resolution NEMO configurations have already proven to be efficient and stable (e.g., Maraldi et al., 2013; Ourmières et al., 2011), but here high-frequency shelf processes as well as seasonal and interannual variability of the water masses are reproduced.

This study has shown that the fine-resolution configuration compares well against the other configurations in terms of the seasonal cycle of sea surface temperature. Though this is not entirely surprising since all configurations have identical surface forcing. For improvement in the small-scale features linked to atmospheric processes (such as wind gusts and local storms), the atmospheric forcing must be taken at finer resolution (Béranger et al., 2010; Bricheno et al., 2013). A significant difference in SST appears, however, in the northern

extent of the domain, where an influx of cold water from the Arctic penetrates into all the configurations and which the AMM60 best reproduces the observed affect in the Faroe-Shetland channel. While the slope current and main dynamics are very similar in all configurations (figure not shown), the finer grid better resolves the complex circulation and eddy field which appears important in determining the water mass pathways in the region of the Norwegian Sea included in the model.

On the shelf, comparison with tide gauges show that the tidal harmonics are not significantly influenced by the increased resolution. This is satisfying not least since the operational class AMM7 has had many person hours optimally tuning its parameters. In comparison with the FASTNEt mooring data, all the configurations reproduced the bulk temperature structure reasonably well. Here however, the AMM60 has anomalously cold bottom water at the shelf break moorings locations. It is noted though that the increased spatial variability in bottom density, associated with the enhanced resolution, could account for the discrepancy seen at fixed moorings (Figure 9b).

For the first time shelf-wide diagnostics of the NW European Shelf semidiurnal internal tide field are presented, highlighting their presence far into the shelf and their dependence on the phase of the spring neap cycle. These baroclinic tides are generated through the interaction between the barotropic tide and the local bathymetry. While NNA and AMM7 can produce internal tides at the severe bathymetric shelf break feature, the grid resolution is not sufficient to simulate their propagation pathways and lifecycles. AMM60, however, can resolve typical interfacial semidiurnal tide wavelengths, and simulate their propagation. In addition, using enhanced resolution demonstrates that internal tides are generated over many small bathymetric features (Figure 9) rather than just at the shelf break or over a few isolated major bathymetric features (e.g., Jones Bank; Palmer et al., 2013). Only a few of these features are large enough to appear in AMM7 and NNA.

This modeling study, which will underestimate the energy in the real fully nonhydrostatic wave field, clearly shows that the internal tide paradigm of planar waves which are primarily generated at the shelf break and propagate on-shelf, (though augmented with isolated and few significant bathymetric source points) is insufficient to describe the complexity of the internal tide wave field. Enhancing the bathymetric roughness from a 7 km to the kilometric scale appears to reveal that many of the bathymetric inhomogeneities are baroclinic tide generators (Baines, 1982) producing a resolvable impact on the pycnocline displacement in much of the domain.

Acknowledgments

This work was supported by the UK NERC funded consortium FASTNEt (NE/I030259/1). In addition J. Polton was supported by NERC standard grant Pycnocline Mixing in Shelf Seas (NE/L003325/1). K. Guihou was supported by the NOC's National Capability Program in Ocean Modelling. This work has used the Centenary Edition of the GEBCO Digital Atlas, published on CD-ROM on behalf of the Intergovernmental Oceanographic Commission and the International Hydrographic Organization as part of the General Bathymetric Chart of the Oceans, British Oceanographic Data Centre, Liverpool, UK. Simulations have been conducted on the ARCHER UK National Supercomputing Service (http://www.archer.ac.uk). The tidal validation and analysis in this manuscript can be reproduced using the tools and open data sets made publicly available under a CECILL license at https://github.com/KarenGuihou/tidal_analysis. The repository contains Python analysis tools to regenerate the tables and figures from data.

References

Arbic, B. K., Wallcraft, A. J., & Metzger, E. J. (2010). Concurrent simulation of the eddying general circulation and tides in a global ocean model. *Ocean Modelling*, *32*, 175–187. https://doi.org/10.1016/j.ocemod.2010.01.007

Baines, P. G. (1982). On internal tide generation models. *Deep Sea Research, Part A. Oceanographic Research Papers*, *29*(3), 307–338. https://doi.org/10.1016/0198-0149(82)90098-X

Béranger, K., Drillet, Y., Houssais, M.-N., Testor, P., Bourdallé-Badie, R., Alhammoud, B., . . . Crépon, M. (2010). Impact of the spatial distribution of the atmospheric forcing on water mass formation in the Mediterranean Sea. *Journal of Geophysical Research*, *115*, C12041. https://doi.org/10.1029/2009JC005648

Bricheno, L. M., Soret, A., Wolf, J., Jorba, O., & Baldasano, J. M. (2013). Effect of high-resolution meteorological forcing on nearshore wave and current model performance. *Journal of Atmospheric and Oceanic Technology*, *30*, 1021–1037. https://doi.org/10.1175/JTECH-D-12-00087.1

Brodeau, L., Barnier, B., Treguier, A.-M., Penduff, T., & Gulev, S. (2010). An era40-based atmospheric forcing for global ocean circulation models. *Ocean Modelling*, *31*, 88–104. https://doi.org/10.1016/j.ocemod.2009.10.005

Dee, D., Uppala, S., Simmons, A. J., Berrisford, P., Poli, P., Kobayashi, S. . . . Vitart, F. (2011). The ERA-Interim reanalysis: Configuration and performance of the data assimilation system. *Quarterly Journal of the Royal Meteorological Society*, *137*, 553–597.

Doodson, A. T. (1921). The harmonic development of the tide-generating potential. *Proceedings of the Royal Society of London, Series A*, *100*(704), 305–329.

Duchez, A., Frajka-Williams, E., Castro, N., Hirschi, J., & Coward, A. (2014). Seasonal to interannual variability in density around the Canary Islands and their influence on the Atlantic meridional overturning circulation at 26°N. *Journal of Geophysical Research: Oceans*, *119*, 1843–1860. https://doi.org/10.1002/2013JC009416

Egbert, G. D., & Bennet, A. F. (1994). TOPEX/POSEIDON tides estimated using a global inverse model. *Journal of Geophysical Research*, *99*(C12), 24821–24852. https://doi.org/10.1029/94JC01894

Egbert, G. D., & Erofeeva, S. Y. (2002). Efficient inverse modeling of barotropic ocean tides. *American Meteorological Society*, *19*, 183–204. https://doi.org/10.1175/1520-0426(2002)019<0183:EIMOBO>2.0.CO;2

Flather, R. A. (1976). A tidal model of the northwest European continental shelf. *Memoires de la Societe Royal des Sciences de Liege*, *10*(6), 141–164.

Frankignoulle, M., & Borges, A. V. (2001). European continental shelf as a significant sink for atmospheric carbon dioxide. *Global Biogeochemical Cycles*, *15*(3), 569–576. https://doi.org/10.1029/2000GB001307

Holt, J., Hyder, P., Ashworth, M., Harle, J., Hewitt, H. T., Liu, H., . . . Wood, R. (2017). Prospects for improving the representation of coastal and shelf seas in global ocean models. *Geoscientific Model Development*, *10*, 499–523. https://doi.org/10.5194/gmd-10-499-2017

Graham, J. A., O'Dea, E., Holt, J., Polton, J., Hewitt, H. T., Furner, . . .Mayorga Adame, C. G. (2017). AMM15: A new high resolution NEMO configuration for operational simulation of the European North West Shelf. *Geoscientific Model Development Discussions.* https://doi.org/10.5194/gmd-2017-127, in press.

Holt, J., & Proctor, R. (2008). The seasonal circulation and volume transport on the northwest European continental shelf: A fine-resolution model study. *Journal of Geophysical Research*, *113*, C06021. https://doi.org/10.1029/2006JC004034

Holt, J., Schrum, C., Cannaby, H., Daewel, U., Allen, I., Artioli, Y., . . . Wakelin, S. (2015). Potential impacts of climate change on the primary production of regional seas: A comparative analysis of five European seas. *Progress in Oceanography*, *140*, 91–115. https://doi.org/10.1016/j.pocean.2015.11.004

Holt, J. T., Allen, J. I., Proctor, R., & Gilbert, F. (2005). Error quantification of a high-resolution coupled hydrodynamic-ecosystem coastal-ocean model: Part 1. Model overview and assessment of the hydrodynamics. *Journal of Marine Systems*, *57*, 167–188. https://doi.org/10.1016/j.jmarsys.2005.04.008

Hopkins, J. E., & Polton, J. A. (2012). Scales and structure of frontal adjustment and freshwater export in a region of freshwater influence. *Ocean Dynamics*, *62*, 45–62. https://doi.org/10.1007/s10236-011-0475-7

Hopkins, J. E., Stephenson, G. R., Green, M. E., Inall, J. A. M., & Palmer, M. R. (2014). Storms modify baroclinic energy fluxes in a seasonally stratified shelf sea: Inertial-tidal interaction. *Journal of Geophysical Research: Oceans*, *119*, 6863–6883. https://doi.org/10.1002/2014JC010011

Howarth, M., & Pugh, D. (1983). *Observations of tides over the continental shelf of northwest Europe* (Vol. 35, chap. 4, pp. 135–143, 145, 147–188). Amsterdam, the Netherlands: Elsevier. https://doi.org/10.1016/S0422-9894(08)70502-6

Huthnance, J. M. (1995). Circulation, exchange and water masses at the ocean margin: The role of physical processes at the shelf edge. *Progress in Oceanography*, *35*(4), 353–431. https://doi.org/10.1016/0079-6611(95)80003-C

Inall, M. E., & the FASTNEt Team. (2012). *D376 cruise report: FASTNEt cruise to the Celtic Sea shelf edge* (Internal Rep. 277). Argyll, UK: SAMS.

Inall, M. E., & the FASTNEt Team. (2013). *Jc88 cruise report: FASTNEt cruise to the Malin Shelf edge* (Internal report). Argyll, UK: SAMS.

IOC. (1985). *M*anual on sea-level measurement and interpretation, *Basic* procedures. *Manuals and guides* (Vol. 1, No. 14, 83 pp.). Paris, France: UNESCO.

Kwong, S. C. M., Davies, A. M., & Flather, R. A. (1997). A three-dimensional model of the principal tides on the European Shelf. *Progress in Oceanography*, *39*, 205–262. https://doi.org/10.1016/S0079-6611(97)00014-1

Large, W. G., & Yeager, S. G. (2004). *Diurnal to decadal global forcing for ocean and sea-ice models: The data sets and flux climatologies* (NCAR Tech. Note NCAR/TN-460+STR). Boulder, CO: National Center for Atmospheric Research.

Lenhart, H. J., Mills, D. K., Baretta-Bekker, H., Van Leeuwen, S. M., Van der Molen, J., Baretta, J. W., . . . Wakelin, S. L. (2010). Predicting the consequences of nutrient reduction on the eutrophication status of the North Sea. *Journal of Marine Systems*, *81*, 148–170. https://doi.org/10.1016/j.jmarsys.2009.12.014

Madec, G. (2008). *NEMO ocean engine* (Tech. Rep. 27). Paris, France: Note du Pole de modelisation, Institut Pierre-Simon Laplace.

Maraldi, C., Chanut, J., Levier, B., Ayoub, N., De Mey, P., Reffray, G., . . . the Mercator Research and Development Team. (2013). NEMO on the shelf: Assessment of the Iberia-Biscay-Ireland configuration. *Ocean Science*, *9*, 745–771. https://doi.org/10.5194/os-9-745-2013

Muller-Karger, F., Varela, R., Thunell, R., Luerssen, R., Hu, C., & Walsh, J. J. (2005). The importance of continental margins in the global carbon cycle. *Geophysical Research Letters*, *32*, L01602. https://doi.org/10.1029/2004GL021346

O'Dea, E. J., Arnold, A. K., Edwards, K. P., Furner, R., Hyder, P., Martin, M. J., . . . Liu, H. (2012). An operational ocean forecast system incorporating NEMO and SST data assimilation for the tidally driven European North-West shelf. *Journal of Operational Oceanography*, *5*(1), 3–17. https://doi.org/10.1080/1755876X.2012.11020128

O'Dea, E. J., Furner, R., Wakelin, S., Siddorn, J. R., While, J., Sykes, P., . . . Hewitt, H. T. (2017). The CO5 configuration of the 7 km Atlantic Margin Model: Large scale biases and sensitivity to forcing, physics options and vertical resolution. *Geoscientific Model Development Discussions*, *10*, 2947–2969. https://doi.org/10.5194/gmd-10-2947-2017

Ourmières, Y., Zakardjian, B., Béranger, K., & Langlais, C. (2011). Assessment of a NEMO-based downscaling experiment for the north-western Mediterranean region: Impacts on the northern current and comparison with ADCP data and altimetry products. *Ocean Modelling*, *39*(3–4), 386–404. https://doi.org/10.1016/j.ocemod.2011.06.002

Palmer, M. R., Inall, M. E., & Sharples, J. (2013). The physical oceanography of jones bank: A mixing hotspot in the Celtic Sea. *Progress in Oceanography*, *117*, 9–24. https://doi.org/10.1016/j.pocean.2013.06.009

Palmer, M. R., Stephenson, G. R., Inall, M. E., Balfour, C., Düsterhus, A., & Green, J. A. M. (2015). Turbulence and mixing by internal waves in the Celtic Sea determined from ocean glider microstructure measurements. *Journal of Marine Systems*, *144*, 57–69. https://doi.org/10.1016/j.jmarsys.2014.11.005

Pinnegar, J. K., Jennings, S., O'Brien, M., & Polunin, V. C. (2002). Long-term changes in the trophic level of the Celtic Sea fish community and fish market price distribution. *Journal of Applied Ecology*, *39*, 377–390. https://doi.org/10.1046/j.1365-2664.2002.00723.x

Polton, J. A. (2015). Tidally induced mean flow over bathymetric features: A contemporary challenge for high-resolution wide-area models. *Geophysical and Astrophysical Fluid Dynamics*, *109*, 207–215. https://doi.org/10.1080/03091929.2014.952726

Porter, M., Inall, M. E., Green, J. A. M., Simpson, J. H., Dale, A. C., & Miller, P. I. (2016). Drifter observations in the summer time Bay of Biscay slope current. *Journal of Marine Systems*, *157*, 65–74. https://doi.org/10.1016/j.jmarsys.2016.01.002

Proctor, R., & James, I. D. (1996). A fine-resolution 3D model of the Southern North Sea. *Journal of Marine Systems*, *8*, 285–295. https://doi.org/10.1016/0924-7963(96)00011-5

Pugh, D. T. (1996). *Tides, surges and mean sea-level (reprinted with corrections)*. Chichester, UK: John Wiley.

Rippeth, T. P. (2005). Mixing in seasonally stratified shelf seas: A shifting paradigm. *Philosophical Transactions of the Royal Society A*, *363*, 2837–2854. https://doi.org/10.1098/rsta.2005.1662

Schrum, C. (1997). Thermohaline stratification and instabilities at tidal mixing fronts: Results of an eddy resolving model for the German bight. *Continental Shelf Research*, *17*, 689–431. https://doi.org/10.1016/S0278-4343(96)00051-9

Sharples, J., Ellis, J. R., Nolan, G., & Scott, B. E. (2013). Fishing and the oceanography of a stratified shelf sea. *Progress in Oceanography*, *117*, 130–139. https://doi.org/10.1016/j.pocean.2013.06.014

Siddorn, J. R., & Furner, R. (2013). An analytical stretching function that combines the best attributes of geopotential and terrain-following vertical coordinates. *Ocean Modelling*, *66*, 1–13. https://doi.org/10.1016/j.ocemod.2013.02.001

Smagorinsky, J. (1963). General circulation experiments with the primitive equations. *Monthly Weather Review*, *91*(3), 99–164.

Stephenson, R. G., Hopkins, J. E., Green, M., Inall, M. E., & Palmer, M. R. (2015). Baroclinic energy flux at the continental shelf edge modified by wind-mixing. *Geophysical Research Letters*, *42*, 1826–1833. https://doi.org/10.1002/2014GL062627

Umlauf, L., & Burchard, H. (2003). A generic length-scale equation for geophysical turbulence models. *Journal of Marine Research*, *61*, 235–265. https://doi.org/10.1357/002224003322005087

Uppala, S. M., Kållberg, P. W., Simmons, A. J., Andrae, U., Bechtold, V. D. C., Fiorino, M., . . . Woollen, J. (2005). The ERA-40 re-analysis. *Quarterly Journal of the Royal Meteorological Society*, *131*(612), 2961–3012. https://doi.org/10.1256/qj.04.176

Vlasenko, V., Stashchuck, N., Inall, M. E., & Hopkins, J. E. (2014). Tidal energy conversion in a global hot spot: On the 3-D dynamics of baroclinic tides at the Celtic Sea shelf break. *Journal of Geophysical Research: Oceans*, *119*, 3249–3265. https://doi.org/10.1002/2013JC009708

Vlasenko, V., Stashchuck, N., Palmer, M. R., & Inall, M. E. (2013). Generation of baroclinic tides over an isolated underwater bank. *Journal of Geophysical Research: Oceans*, *118*, 4395–4408. https://doi.org/10.1002/jgrc.20304

Vörösmarty, C. J., Fekete, B. M., Meybeck, M., & Lammers, R. B. (2000). Global system of rivers: Its role in organizing continental land mass and defining land-to-ocean linkages. *Global Biogeochemical Cycles*, *14*(2), 599–621. https://doi.org/10.1029/1999GB900092

Welch, P. D. (1967). The use of fast Fourier transform for the estimation of power spectra: A method based on time averaging over short, modified periodograms. *IEEE Transactions on Audio and Electroacoustics*, *15*(2), 70–73.

Xing, J., & Davies, A. M. (2002). Processes influencing the non-linear interaction between inertial oscillations, near inertial internal waves and internal tides. *Continental Shelf Research*, *29*, 1067. https://doi.org/10.1029/2001GL014199